



**HAL**  
open science

## CorPhU: an algorithm based on phase closure for the correction of unwrapping errors in SAR interferometry

Angélique Benoit, Béatrice Pinel-Puysségur, Romain Jolivet, Cécile Lasserre

### ► To cite this version:

Angélique Benoit, Béatrice Pinel-Puysségur, Romain Jolivet, Cécile Lasserre. CorPhU: an algorithm based on phase closure for the correction of unwrapping errors in SAR interferometry. *Geophysical Journal International*, 2020, 221 (3), pp.1959-1970. 10.1093/gji/ggaa120 . hal-02152196v2

**HAL Id: hal-02152196**

**<https://hal.science/hal-02152196v2>**

Submitted on 26 Mar 2020

**HAL** is a multi-disciplinary open access archive for the deposit and dissemination of scientific research documents, whether they are published or not. The documents may come from teaching and research institutions in France or abroad, or from public or private research centers.

L'archive ouverte pluridisciplinaire **HAL**, est destinée au dépôt et à la diffusion de documents scientifiques de niveau recherche, publiés ou non, émanant des établissements d'enseignement et de recherche français ou étrangers, des laboratoires publics ou privés.

# CorPhU: an algorithm based on phase closure for the correction of unwrapping errors in SAR interferometry

Angélique Benoit<sup>1</sup>, Béatrice Pinel-Puysségur<sup>2</sup>, Romain Jolivet<sup>1</sup> and Cécile Lasserre<sup>3</sup>

<sup>1</sup> Laboratoire de Géologie, Département de Géosciences, Ecole Normale Supérieure, PSL University, UMR CNRS 8538, Paris, France, [angelique.benoit@ens.fr](mailto:angelique.benoit@ens.fr).

<sup>2</sup> CEA, DAM, DIF, F-91297 Arpajon, France.

<sup>3</sup> Université de Lyon, UCBL, ENSL, CNRS, LGL-TPE, 69622 Villeurbanne, France.

Accepted: XXX; Received XXX; in original form XXX

1 Interferometric Synthetic Aperture Radar is commonly used in Earth Sciences to  
2 study surface displacements or construct high resolution topographic maps. Recent  
3 satellites such as those of the Sentinel-1 constellation allow to derive dense deforma-  
4 tion maps with millimetric precision with high revisit frequency. However, InSAR is  
5 still limited by interferometric coherence. Interferometric phase noise resulting from  
6 a loss of coherence, due to changes in scattering properties between repeated SAR ac-  
7 quisitions, may lead to unwrapping errors, which then in turn lead to centimetric errors  
8 in time series reconstruction. We present an algorithm based on interferometric phase  
9 closure to automatically correct unwrapping errors. We describe the algorithm and  
10 highlight its performances with two case studies, in Lebanon with Envisat satellite data  
11 and in Central Turkey with Sentinel-1 data. The first dataset is particularly affected  
12 by unwrapping errors because of long spatial (500 m) and temporal baseline interfero-  
13 grams (6 years) and decorrelation due, in particular, to vegetation. The second dataset  
14 contains unwrapping errors because of temporal changes in the scattering properties  
15 of the ground. For these two examples, the algorithm allows the correction of almost  
16 all detectable unwrapping errors, without requiring visual inspection or manual dele-  
17 tions. Our algorithm is efficient especially on large datasets, such as with Sentinel-1

18 constellation, where interferometric phase is redundant and improves eventually the  
19 reconstruction of time series.

20

21 Radar interferometry – Image processing – Creep and deformation.

## 22 **1 Introduction**

23 Interferometric Synthetic Aperture Radar (InSAR) is a geodetic technique developed  
24 in the 70's for geophysical applications and, originally, to construct topographic maps  
25 of the Earth (Graham, 1974; Zebker & Goldstein, 1986), Venus (Rogers & Ingalls,  
26 1970) and the Moon (Zisk, 1972a,b; Margot et al., 2000). In the 90's, InSAR was then  
27 used for the study of surface displacements related to earthquakes (Massonnet et al.,  
28 1993; Zebker et al., 1994), inflation of volcanoes (Massonnet et al., 1995) or ice sheet  
29 motion (Goldstein et al., 1993). InSAR is based on the acquisition of successive SAR  
30 images over the same area and from close positions by a side looking radar onboard  
31 a plane or a satellite. The complex conjugate product of two SAR images is called  
32 an interferogram. The phase of an interferogram, hereafter called the interferometric  
33 phase, corresponds to the relative travel time difference of the electromagnetic wave  
34 between two SAR acquisitions. The interferometric phase depends on satellite orbits,  
35 topography, spatio-temporal variations in the refractive index of the atmosphere be-  
36 tween two acquisitions, ground deformation along the satellite line-of-sight (LOS) and  
37 various sources of noise, including Digital Elevation Model, orbits errors and instru-  
38 mental noise. With two simultaneous acquisitions from two points of view, InSAR is a  
39 measurement of topography used to build DEMs, while with successive acquisitions it  
40 can be used to measure ground deformation. Measurements of deformation and ground  
41 velocity using InSAR have now reached a millimeter accuracy (Simons & Rosen, 2015;  
42 Elliott et al., 2016).

43 Reconstructing continuous signals, including deformation, involves phase unwrap-

44 ping, which consists in adding the appropriate multiple of  $2\pi$  to the interferometric  
45 phase and multiple methods have been developed to do so. Branch-cut algorithms  
46 consist in identifying consistent and inconsistent paths to integrate the phase signal  
47 (Goldstein et al., 1988; Prati et al., 1990; Lin et al., 1994; Hertzberg et al., 2018).  
48 Least-squares techniques, weighted or unweighted, minimize the mean deviation be-  
49 tween the estimated (wrapped) and unknown (unwrapped) discrete derivatives of the  
50 phase (Ghiglia & Romero, 1994; Flynn, 1997; Costantini, 1998; Chen & Zebker, 2001),  
51 sometimes using external data such as GPS to constrain the unwrapping process (Agram  
52 & Zebker, 2010). Ultimately, Permanent or Persistent Scatterers InSAR (PS-InSAR)  
53 methods, based on the identification of pixels with stable backscattering properties in  
54 time, use the temporal information of multiple interferograms to unwrap the phase in  
55 time and space (Pepe & Lanari, 2006; Hooper & Zebker, 2007; Hussain et al., 2016).

56 However, phase unwrapping may fail, especially within low coherence regions  
57 (Rosen et al., 1996). In an interferogram, each pixel phase value corresponds to the  
58 phase of the coherent sum of backscattered electromagnetic wave from scatterers on  
59 the ground within the pixel. If scattering properties change over time or if the geome-  
60 try of acquisition is too different between each pass of the satellite, the phase change  
61 between two neighbouring pixels may exceed one phase cycle (i.e.  $2\pi$ ). Coherence  
62 is a measure of the spatial correlation of phase (Lee et al., 1994). A coherence of 1  
63 indicates the phase is constant within a cell surrounding the pixel. Over low coherence  
64 regions, higher phase noise may lead to phase differences between neighbouring pixels  
65 higher than  $\pi$ . In addition, large deformation gradients may lead to similar situation,  
66 for instance close to a fault that ruptured in a large seismic rupture (e.g. Simons et al.,  
67 2002).

68 Phase unwrapping is based on the hypothesis that the phase of two neighbouring  
69 pixels of an interferogram only differs by a fraction of  $\pi$ . This hypothesis is only valid  
70 in high coherence regions with a moderate fringe rate. When this assumption breaks

71 down, unwrapping methods may fail, creating erroneous offsets of multiples of  $2\pi$  in  
72 the unwrapped phase. The size of the affected region may vary from a few pixels  
73 to a significant fraction of the image. In Earth science applications, almost all inter-  
74 ferograms have large regions where phase decorrelates due to changes in scattering  
75 properties (e.g. vegetation, humidity, anthropic changes), high topographic gradients  
76 or high deformation areas and unwrapping becomes challenging (Simons et al., 2002;  
77 Zebker et al., 2007). Unwrapping errors bias estimations of surface deformation by in-  
78 troducing inconsistencies in the interferometric network in case of time series analysis.  
79 Unwrapping errors are sometimes manually detected and masked (e.g. Jolivet et al.,  
80 2012) and methods based on interferometric network misclosure analysis (e.g. López-  
81 Quiroz et al., 2009) and time series analysis have been proposed (e.g. Hussain et al.,  
82 2016).

83 We propose an efficient algorithm, named CorPhU (CORrection of Phase Unwrap-  
84 ping errors), for the correction of unwrapping errors after phase unwrapping, based on  
85 the phase closure of interferogram triplets within an interferometric network. A proof  
86 of concept of this algorithm has been presented by Pinel-Puysségur et al. (2018) and we  
87 describe in details the formulation, implementation and performances of the algorithm  
88 in this paper. Phase unwrapping errors detected by the algorithm are automatically and  
89 iteratively corrected. In the following sections, we describe the algorithm and present  
90 qualitative results focusing on two case studies where decorrelation is high and could  
91 be a limiting factor, including data from the Envisat satellite over Lebanon and data  
92 from the Sentinel-1 constellation over Turkey. We then perform a quantitative assess-  
93 ment of the algorithm. Finally, we discuss limitations and possible improvements of  
94 our approach.

## 95 **2 Method**

96 By construction, the sum of the phase of three unwrapped interferograms forming a  
97 closed loop equals 0 (Jennison, 1958). For a triplet  $T$  of three SAR acquisitions  $k$ ,  $l$   
98 and  $m$ , the triplet phase closure  $\Phi_T$  is:

$$\Phi_T = \phi_{kl} + \phi_{lm} - \phi_{km}, \quad (1)$$

99 where  $\phi_{kl}$ ,  $\phi_{lm}$  and  $\phi_{km}$  are the unwrapped phase of interferograms  $I_{kl}$ ,  $I_{lm}$  and  $I_{km}$   
100 computed from acquisitions  $k$ ,  $l$  and  $m$ . By construction, phase closure  $\Phi_T$  should be  
101 equal to 0, up to phase inconsistencies due to variations of the backscattering proper-  
102 ties of the ground, including for instance soil moisture (De Zan et al., 2015). Once  
103 this later contribution is removed, the remaining phase closure inconsistencies corre-  
104 spond to phase unwrapping errors exactly equal to a multiple of  $2\pi$ . Our algorithm de-  
105 tects and corrects such unwrapping errors within a stack of coregistered interferograms  
106 formed from SAR images (Fig. 1). First, we identify all triplets in the interferogram  
107 network. Second, we compute the phase closure for each triplet following equation  
108 1 and identify unwrapping errors. Third, for each of these incorrectly unwrapped re-  
109 gions, we identify the interferogram incorrectly unwrapped among the three possible  
110 ones using the so-called “flux” or “mean closure” methods, described in sections 2.2  
111 and 2.3 respectively. Once we have identified the interferogram incorrectly unwrapped,  
112 we correct the unwrapping error. We proceed iteratively through the network of triplets.

### 113 **2.1 Automatic identification of unwrapping errors**

114 For all available triplets, we start by building masks  $m_{kl}$ ,  $m_{lm}$  and  $m_{km}$  associated  
115 to interferograms  $I_{kl}$ ,  $I_{lm}$  and  $I_{km}$ , based on the coherence map. Pixels with a co-  
116 herence lower than a given threshold (0.8 by default) are masked out. If none of the  
117 three individual masks is empty, we construct the total mask of the triplet  $m_T^{tot}$  as the

118 intersection of masks  $m_{kl}$ ,  $m_{lm}$  and  $m_{km}$ . We then compute triplet closure on un-  
 119 wrapped interferograms using equation 1. We distinguish two sources of misclosure  
 120 in unwrapped interferograms. The first one is unwrapping errors and is specific to un-  
 121 wrapped interferograms. The second one arises from interferogram multilooking prior  
 122 to unwrapping. Indeed, multilooking is a non-coherent summation of different pix-  
 123 els, leading to small phase inconsistencies in the wrapped interferograms and thus to  
 124 non-zero closure (De Zan et al., 2015). We therefore calculate the closure of wrapped  
 125 interferograms, defined as:

$$\Phi_T^w = (\phi_{I_{kl}}^w + \phi_{I_{lm}}^w - \phi_{I_{km}}^w)[2\pi], \quad (2)$$

126 where  $\phi_{kl}^w$ ,  $\phi_{lm}^w$  and  $\phi_{km}^w$  are the phase of wrapped interferograms computed from ac-  
 127 quisitions  $k$ ,  $l$  and  $m$  and modulo  $[2\pi]$  indicates phase signals are within the interval  
 128  $[0; 2\pi]$ . We subtract closure of wrapped interferograms  $\Phi_T^w$  from closure  $\Phi_T$  com-  
 129 puted on unwrapped interferograms in order to remove misclosures related to phase  
 130 consistency loss in multilooking (Eq. 3, Fig. 2). The total triplet closure  $\Phi_T^{tot}$  hence  
 131 writes:

$$\Phi_T^{tot} = (\Phi_T - \Phi_T^w)m_T^{tot}. \quad (3)$$

132 We then round the total triplet closure  $\Phi_T^{tot}$  modulo  $2\pi$  to estimate how many multi-  
 133 ples of  $2\pi$  should be corrected. We consider non-zero values as unwrapping errors and  
 134 group them into regions using structuring elements (Fig. 3b; Verveer, 2003). Remain-  
 135 ing zero-values (i.e. pixel has been correctly unwrapped) are grouped into regions,  
 136 considered as reference for the flux method described in the next section. Phase un-  
 137 wrapping errors generally arise in noisy or high fringe rate areas on interferograms.  
 138 The error spreads from this area, forming a connected region on which phase has been  
 139 locally correctly unwrapped but is inconsistent with neighbouring regions. We then  
 140 associate each unwrapping error region to the largest reference region in the vicinity.

141 Now that we know where each unwrapping error is, we need to determine which in-  
142 terferogram of the triplet has been incorrectly unwrapped using a two-steps detection  
143 approach.

## 144 **2.2 Step 1: flux method selection**

145 We first try to identify which interferogram of a triplet shows an abnormal phase off-  
146 set, called “flux”, between an unwrapping error and its associated reference region. To  
147 compute this flux, we need to both erode and dilate the incorrectly unwrapped region  
148 to respectively isolate pixels within the unwrapping error from outside adjacent pixels,  
149 which are within a reference region (i.e. phase closure equals to zero). As explained in  
150 details in [Pinel-Puysségur et al. \(2018\)](#), we first fill up masked pixels within the error  
151 region (Figs 3b and c; [Verveer, 2003](#)) and we erode and dilate using a structuring ele-  
152 ment, here chosen as a square of 2x2 pixels ([Matheron, 1967](#)). The difference between  
153 the dilated and the original regions determines the outer border of the unwrapping er-  
154 ror. Similarly, the difference between the eroded and the original regions determines  
155 the inner border of the unwrapping error (Fig. 3d). The size of the structuring element  
156 used for erosion and dilatation has been empirically chosen for the borders to be thin  
157 enough to compute the flux between neighbouring pixels but wide enough to ensure a  
158 sufficient number of flux measurements. We then discard pixels of the inner border that  
159 do not have any neighbour in the outer border, for example when they are on the image  
160 border, close to a masked region or far from the reference region. We calculate flux  
161 vectors along this boundary by differencing the phase of an inner pixel with the phase  
162 of the neighbouring outer pixel (Fig. 3e). We define  $p_{flux}$  as the minimum proportion  
163 of flux vectors to correct an interferogram. For each interferogram of a triplet, we esti-  
164 mate the proportion of flux vectors equal to a multiple of  $2\pi$ . If only one interferogram  
165 has more than  $p_{flux}$  of its flux vectors equal to a multiple of  $2\pi$ , this interferogram is  
166 marked as incorrectly unwrapped and the error is corrected by adding the appropriate



167 multiple of  $2\pi$ . If two or three interferograms have a proportion greater than  $p_{flux}$ ,  
 168 we cannot discriminate which interferogram is to be corrected. In our case,  $p_{flux}$  is  
 169 set to 30%. This choice is empirical and based on a user decision. In our two case  
 170 studies, if  $p_{flux}$  is too small (i.e. we have very few flux vectors), the algorithm misses  
 171 the interferogram to correct.

### 172 **2.3 Step 2: mean closure method selection**

173 If the flux method cannot determine which interferogram has to be corrected, we try to  
 174 identify the interferogram incorrectly unwrapped by computing the mean closure of the  
 175 three interferograms for all their triplets. We consider interferogram  $I_{kl}$  that belongs  
 176 to  $N_{I_{kl}}$  triplets. The mean closure of interferogram  $I_{kl}$ , noted  $\Phi_{I_{kl}}^{mean}$ , is defined as the  
 177 sum of the phase closure  $\Phi_n$  on its  $N_{I_{kl}}$  triplets, normalized by the number of triplets  
 178  $N_{I_{kl}}$ :

$$\Phi_{I_{kl}}^{mean} = \frac{\sum_{n=1}^{N_{I_{kl}}} \Phi_n}{m_{I_{kl}}} M_{I_{kl}}, \quad (4)$$

179 where  $M_{I_{kl}}$  is the intersection of all masks associated to each triplet and  $m_{I_{kl}}$  is an  
 180 image containing for each pixel the number of defined triplets (without mask) for inter-  
 181 ferogram  $I_{kl}$ . We define  $p_{mc}$  as the minimum proportion of pixels equal to a multiple  
 182 of  $2\pi$  to correct an interferogram. For each interferogram of the triplet, we compute  
 183 the proportion of pixels in the unwrapping error zone such that the mean closure is  
 184 equal to a multiple of  $2\pi$ . If only one interferogram has more than  $p_{mc}$  pixels equal  
 185 to a multiple of  $2\pi$  in the unwrapping error region, this one is marked as incorrectly  
 186 unwrapped and the error is corrected. If two interferograms fulfill this condition and  
 187 if the ratio between the two proportions, noted  $r_{mc}$ , is greater than 2 (by default), the  
 188 interferogram of highest proportion is corrected. Otherwise, we cannot discriminate  
 189 which interferogram to correct. As the error may be corrected in another triplet, the  
 190 algorithm then processes the following triplet. In our case studies,  $p_{mc}$  is set to 50%, a

191 number that has been found empirically to increase the reliability of corrections. This  
192 threshold should be chosen on a case-by-case basis and is region dependent.

193

194 In general, the algorithm should be iteratively run multiple times until no unwrap-  
195 ping corrections are needed. Several parameters such as the size of the structuring  
196 element used for dilation and erosion and threshold values may influence the perfor-  
197 mances of the algorithm. Users have to determine which set of parameters provides  
198 adequate unwrapping error corrections for each dataset. We propose in the following  
199 to evaluate the performance of our method and provide guidelines on how to chose  
200 various parameters.

### 201 **3 A qualitative examination on two case studies**

202 We experiment our algorithm on two sets of SAR acquisitions and present the effects  
203 of unwrapping errors on time series analysis. First, we process the archive of SAR  
204 acquisitions from the Envisat C-Band satellite over Lebanon. There, unwrapping errors  
205 arise because of low phase coherence due to interferograms with long perpendicular  
206 baselines (max. perpendicular baseline: 500 m; max. temporal baseline: 6 years)  
207 and to the presence of vegetation. Second, we process SAR acquisitions from the  
208 constellation of Sentinel-1 C-Band satellites over Central Turkey (max. perpendicular  
209 baseline: 250 m; max. temporal baseline: 1 year). This constellation offers a much  
210 shorter revisit time and a larger coverage compared to products from Envisat (revisit  
211 time of 6 days, 300 km wide). Manual corrections of unwrapping errors cannot be  
212 performed because of the untractable size of the resulting dataset. The two case studies  
213 below differ by satellites and processing approach, however, both aim at retrieving  
214 slow tectonic deformations. As we are attempting to measure slow deformation rates  
215 at a regional scale and because of strong decorrelation effects, due for example to  
216 residual atmospheric artefacts, vegetation and snow in the winter, strong multilooking

217 is required to enhance coherence in both cases, otherwise unwrapping of the phase is  
218 almost impossible.

### 219 **3.1 Application to Envisat dataset in Lebanon**

220 The Levant fault system is a complex active fault system of 1200 kilometers-long,  
221 where large earthquakes of magnitude up to 7.5 occurred in the past (e.g. [Elias et al.,](#)  
222 [2007](#)). This major continental fault bounds the Arabian and African plates.

223 We process data from Envisat ASAR track 78 with NSBAS ([Doin et al., 2011](#)),  
224 a processing chain based on the Repeat Orbit Interferometry PACKage (ROIPAC)  
225 ([Rosen et al., 2004](#)). We coregister SLCs to a master image taking into account lo-  
226 cal topography ([Guillaso et al., 2008](#)). We use DORIS orbits from the European  
227 Space Agency (ESA) and SRTM Digital Elevation Model (DEM) Version 3.0 ([Farr](#)  
228 [et al., 2007](#)) to compute the orbital and topographic phase contributions. We multi-  
229 look wrapped interferograms by a factor of 4 in range and 20 in azimuth. We use  
230 MuLSAR (Multi-Link Interferograms) in order to increase the signal-to-noise ratio of  
231 interferograms ([Pinel-Puysségur et al., 2012](#)). We then correct wrapped interferograms  
232 from stratified tropospheric delays estimated from the ERA-Interim global atmospheric  
233 reanalysis from ECMWF ([Doin et al., 2009](#); [Jolivet et al., 2011](#)). We evaluate and com-  
234 pensate DEM errors by estimating the bias induced by perpendicular baselines ([Ducret](#)  
235 [et al., 2014](#)). Finally, we filter interferograms using a Goldstein filter ([Goldstein &](#)  
236 [Werner, 1998](#)), multilook by an additional factor of 4 (16 looks in range, 80 looks in  
237 azimuth) and unwrap them using the branch-cut method ([Goldstein et al., 1988](#)). Our  
238 final dataset is made of 165 unwrapped interferograms.

239 Our algorithm identifies 282 triplets, among which 186 are corrected. We illustrate  
240 automatic corrections with a long temporal baseline interferogram, spanning 4 years,  
241 where three corrections are performed (Fig. 4). The first error (number 1 in Fig. 4)  
242 is clearly well corrected. The two other errors (number 2 and 3 in Fig. 4) are more

243 challenging due to the effect of filtering on high fringe rate areas. In both cases, a  
244 sharp fringe, partially visible on the interferogram before filtering (arrows in Fig. 4d  
245 and f), disappears through filtering (arrows in Fig. 4e and g) hence leading to disconti-  
246 nities in the unwrapped interferograms (red circles in Fig. 4b). After correction, the  
247 algorithm restores continuity where a  $2\pi$  phase offset was inconsistently introduced by  
248 the unwrapping procedure (red circles in Fig. 4c) and discontinuity in high fringe rate  
249 areas (arrows in Fig. 4c).

### 250 **3.2 Application to Sentinel-1 dataset in Central Turkey**

251 The North Anatolian Fault is an active right-lateral strike-slip fault that accommodates  
252 the rotation of Anatolia with respect to Eurasia. During the 19<sup>th</sup> century, seismic ac-  
253 tivity was characterized by a westward propagation of large earthquakes ( $\sim M_W$  7.0)  
254 along this 1200 kilometers-long fault (Stein et al., 1997). The last earthquake to date  
255 is the Izmit event  $M_W$  7.5 in 1999, east of the Sea of Marmara (e.g. Reilinger et al.,  
256 2000).

257 We process data from Sentinel-1 track 87 with the InSAR Scientific Computing En-  
258 vironment (ISCE) software (Gurrola et al., 2010). We define the acquisition of July, 9<sup>th</sup>  
259 2017 as the master Single Look Complex (SLC) and coregister all SLCs to this master  
260 image. Coregistration is enhanced using the spectral diversity of burst overlaps refined  
261 within the network of interferograms (Fattahi et al., 2017). We generate interfero-  
262 grams, accounting for digital elevation model (SRTM Version 3.0; Farr et al., 2007)  
263 and orbital contributions, and merge tiles for each of them using bursts and swaths  
264 overlaps. We multilook merged interferograms with factors of respectively 81 and 27  
265 in azimuth and range directions for a final pixel size of 540 x 420 meters, in range and  
266 azimuth respectively. We correct the phase from tropospheric signals using ERA-5, the  
267 latest global atmospheric reanalysis from ECMWF (Hersbach & Dee, 2016). Finally,  
268 we filter (Goldstein & Werner, 1998) and unwrap interferograms using the branch-cut

269 method (Goldstein et al., 1988). Before building triplets, we discard low coherence in-  
270 terferograms which cannot be sufficiently unwrapped (less than 20% of the area). Our  
271 final dataset is made of 686 coregistered and unwrapped interferograms.

272 Our algorithm identifies 2880 triplets, among which 986 triplets are corrected even-  
273 tually (Fig. 5a). We calculate the percentage of corrected pixels per interferogram by  
274 summing the number of pixels detected as unwrapping errors and corrected by the al-  
275 gorithm in all triplets of the interferogram. We see that most of the interferograms are  
276 totally corrected from unwrapping errors during a first pass of the algorithm (Fig. 5b).  
277 We illustrate automatic corrections with two examples of corrected interferograms, one  
278 with a large unwrapping error of 10388 pixels (4% of the interferogram, Fig. 5c) and  
279 another with two unwrapping errors localized in different places (Fig. 5d). In both  
280 cases, 99% of the unwrapping error is automatically detected and corrected by the  
281 algorithm. Uncorrected pixels are located in the masked region of the triplet. The  
282 second example shows that the algorithm can perform multiple corrections in a single  
283 interferogram (Fig. 5d). In this case, it detects two unwrapping errors in the same  
284 interferogram and corrects them in the same triplet.

## 285 **4 Discussion and quantitative tests**

### 286 **4.1 Unwrapping errors and time series analysis**

287 One potential application of SAR interferometry is to perform time series analysis  
288 and estimate ground velocity over a given region from a stack of interferograms. We  
289 illustrate the effect of automatic corrections of unwrapping errors on the estimation of  
290 ground velocity and the associated decrease in errors on ground surface deformation  
291 measurement.

292 We perform two time series analysis on the Sentinel-1 dataset (Section 3.2): the  
293 first one is applied to the original stack of interferograms not corrected from unwrap-

294 ping errors, the second one is applied to the interferograms corrected by the proposed  
295 approach. We invert the temporal evolution of the phase for both datasets identically us-  
296 ing the small baseline NSBAS approach (Doin et al., 2011) implemented in the Generic  
297 InSAR Analysis Toolbox (GIAnt) (Agram et al., 2012). In this method, we consider  
298 each pixel independently to recover the phase change with time (López-Quiroz et al.,  
299 2009; Doin et al., 2011; Jolivet et al., 2012). In addition to phase reconstruction, NS-  
300 BAS includes a time dependent model of the phase to predict the phase evolution with  
301 time when interferometric links are missing between two disconnected subsets of in-  
302 terferograms.

303 For each time series analysis, we first remove interferograms that have less than  
304 35% unwrapped pixels, hence reducing the dataset to 627 interferograms. We then  
305 multilook interferograms by a factor of 2 in order to reduce noise on the interferograms  
306 (due to the presence of vegetation and snow) and spatially reference them by choosing  
307 a region where the phase is set to be equal in all interferograms. We correct orbital  
308 biases in interferograms by estimating a linear ramp. Terms of the ramp are refined  
309 accounting for the interferometric network (Lin et al., 2010; Jolivet et al., 2012). We  
310 then perform a least squares inversion of phase delays of each pixel to solve for the  
311 total phase delay of each date relative to the first date and for a parametric evolution of  
312 phase change across the whole acquisition period. The parametric evolution of surface  
313 deformation is a combination of a linear term and a seasonal-annual function.

314 We obtain two velocity maps over Central Turkey (Fig. 6a and b). If we do not  
315 correct interferograms from unwrapping errors before the inversion, surface velocity is  
316 strongly affected by unwrapping errors (Fig. 6a, b, d and e). In particular, several sus-  
317 picious discontinuities visible on the first velocity map (Fig 6a and 6d) are not detected  
318 on the second one (Fig 6b and 6e). The difference in velocity between the two fields  
319 reaches up to 4 mm/yr in large regions (Fig. 6c), corresponding in our case to about  
320 20% of the expected tectonic displacement in the area. We can also identify small dif-

321 ferences of about 1 mm/yr (Fig. 6c and f), due to a difference in referencing between  
 322 the two velocity maps. If we choose a reference region within an unwrapping error, the  
 323 inversion will differ hence the resulting velocity maps will be different.

324 The effect of unwrapping errors can be evaluated quantitatively by computing a  
 325 Root Mean Square (RMS) map, defined as:

$$\Phi_{RMS} = \frac{1}{N} \left[ \sum_N \left( \phi_{ij} - \sum_{k=i}^{j-1} m_k \right)^2 \right]^{1/2}, \quad (5)$$

326 where  $\phi_{ij}$  is the measured phase between acquisitions  $i$  and  $j$  and  $\sum_{k=i}^{j-1} m_k$  is the re-  
 327 constructed phase between the same acquisitions (Fig. 7; [Cavalié et al., 2007](#)). This  
 328 RMS evaluates the quality of the time series reconstruction and should then reflect in-  
 329 terferometric misclosure. If we do not correct interferograms from unwrapping errors  
 330 before the inversion, RMS reaches 12 mm (Fig. 7a), compared to few millimeters if  
 331 unwrapping errors are corrected with the proposed approach (Fig. 7c). Average RMS  
 332 is of 1.61 mm without corrections and 0.98 mm with corrections. In the case where  
 333 unwrapping errors are not corrected, deviation in RMS is much larger than when er-  
 334 rors are corrected, with extreme values of 8 to 14 mm (Fig. 7b). Since pixels with a  
 335 large RMS after time series analysis cannot be trusted for further interpretation, our  
 336 approach allows to extend the area over which we can interpret the LOS displace-  
 337 ment signal. Therefore, correcting unwrapping errors allows to expand the zone over  
 338 which we confidently measure ground velocity, in the present case by 20% with a RMS  
 339 threshold of 3 mm.

## 340 4.2 Parametric tests on the Lebanon dataset

341 The validation of an automatic correction algorithm for phase unwrapping errors is a  
 342 difficult task. The ideal way to assess the performance of such an algorithm would  
 343 be to have a comprehensive ground truth where every pixel of every interferogram of

344 the database is labelled as correctly or incorrectly unwrapped. Then, for each pixel  
345 incorrectly unwrapped, the number of cycles of the error and its associated sign should  
346 be known. In addition, such ground truth would allow identifying false alarms, i.e.  
347 pixels correctly unwrapped but detected as incorrectly unwrapped.

348 Practically, on a real database, there is no simple and efficient way to determine  
349 which pixels have been incorrectly unwrapped. It should be stressed that pixels in-  
350 correctly unwrapped may be detected easily on a triplet thanks to its closure but that  
351 determining them directly on interferograms is a tedious task. Indeed, even a thorough  
352 visual examination of interferograms does not always allow determining if a region is  
353 incorrectly unwrapped and if so to which extent. Furthermore, no independent dataset  
354 provides comparable measurement at the resolution allowed by InSAR.

355 There are two strategies to quantitatively validate the results of the proposed al-  
356 gorithm. The first one is to establish an experimental ground truth on a part of a real  
357 database by visual inspection. The second one would be to create a synthetic database  
358 on which unwrapping errors would be known. This last one will be explored in fu-  
359 ture work. In this paper, we chose to derive quantitative performances attempting to  
360 compare with our experimental ground truth.

361 Because we need to identify manually unwrapping errors, we will apply our val-  
362 idation on the Lebanon dataset. We select 22 interferograms with easily identifiable  
363 unwrapping errors. For each interferogram, we manually detect and label the regions  
364 of unwrapping errors. For each region, we also identify the signed number of phase  
365 cycles of the error. We thoroughly perform this manual task to ensure that the exper-  
366 imental ground truth does not contain any error. The ground truth contains 26 error  
367 regions with a total of 120235 pixels. To check if the algorithm detects false alarms,  
368 we select 15 interferograms and manually cut out and store regions that do not contain  
369 any unwrapping errors, with a total of 983310 pixels.

370 CorPhU depends on four parameters (see Table 1). Instead of a full parametric



371 study which is beyond the scope of this paper, we focus our parametric tests on two out  
372 of the four parameters identified as the most important ones, including the thresholds  
373  $p_{flux}$  and  $p_{mc}$  used for the identification of the incorrectly unwrapped interferogram  
374 of a triplet.

375  $p_{flux}$  and  $p_{mc}$ , two proportions of flux or pixels, are defined between 0 and 100%.  
376 For the parametric tests, we test values ranging from 10% and 90% with a step of 20%.  
377 We also test the algorithm with only one of the two steps. To do so, we set  $p_{flux}$  (resp.  
378  $p_{mc}$ ) to a value strictly greater than 100%. As a proportion would never attain such  
379 a value, we only use the 2<sup>nd</sup> step (resp. 1<sup>st</sup> step) during the run. In practice, the case  
380 with both  $p_{flux}$  and  $p_{mc}$  strictly greater than 100% prohibits any correction and is not  
381 applicable.

382 We run CorPhU with each of these combinations on the whole Lebanon dataset,  
383 with two iterations. We then compute the True Detection (TD) and False Alarm (FA)  
384 rates on the ground truth as follows. For each region labelled as incorrectly unwrapped  
385 in the ground truth, we compute the difference between the interferogram obtained after  
386 CorPhU's processing and the original one. We compare this difference to the expected  
387 correction, which is known from our estimates of ground truth. If these quantities are  
388 equal, then the error region has been well detected. Then, we compute the ratio of well  
389 detected regions as the TD rate. For the FA rate, we compare all regions of the ground  
390 truth labelled as correctly unwrapped to the difference of the interferograms before and  
391 after CorPhU's processing. This difference should be zero. If not, we count the region  
392 as a FA.

393 The results do not show any sufficient variation as a function of the parameters. For  
394 almost every test, the TD rate is quasi constant between 46% and 50%. The only cases  
395 where the TD rate decreases significantly (under 40%) are for  $p_{mc}$  or  $p_{flux}$  strictly  
396 greater than 100% (only one of the steps is used). Similarly, the FA rate is almost  
397 always equal to 0 except for some cases where it reaches 2%. These results do not

398 sufficiently vary to draw any conclusion on the influence of the parameters. However,  
399 we can draw two conclusions.

400 First, only half of unwrapping errors of this particular ground truth are detected.  
401 This poor performance can be explained as follows. In the Lebanon test case, there are  
402 only 282 triplets for 165 interferograms or an average of 1.71 triplets per interferogram.  
403 Moreover, many interferograms are partially masked. As triplet closure is only defined  
404 on the intersection of the definition domain of the three interferograms, the effective  
405 number of triplets per interferogram is even strictly smaller than 1.71. CorPhU should  
406 work better when the number of triplets increases for several reasons: first, the errors  
407 can only be detected on triplets closures; second, the first step needs a neighboring  
408 reference region on which the triplet closure is defined; third, the second step needs at  
409 least two triplets per interferogram under examination to determine which one is badly  
410 unwrapped. The poor TD rate on this database could thus be explained by the lack of  
411 triplets and the large masked areas, especially compared to the Turkey dataset where  
412 an interferogram belongs to 8.2 triplets on average.

413 Second, we think our estimate of ground truth is not sufficient and not precise  
414 enough to assess the parameters influence on CorPhU’s performances. It highlights  
415 the need of a synthetic database where the number of interferograms and triplets, the  
416 masked areas surface or other variables could be changed and their effect on CorPhU’s  
417 performances properly assessed.

418 Consequently, we choose to assess the influence of tunable parameters on the per-  
419 formance by counting the number of pixels incorrectly unwrapped before and after the  
420 run. We automatically compute the total number of pixels on all triplets with non-zero  
421 triplet closure,  $W$ . We then derive the difference  $\Delta W$  between  $W$  before ( $W_{init}$ ) and  
422 after ( $W_{final}$ ) the run to derive the percentage of corrected pixels (here,  $W_{init}$  is equal  
423 to 1847173 pixels, see Table 2) .

424 Table 2 shows that the percentage of corrected pixels highly depends on the pa-

425 parameter value. We highlight in green in Table 2 the range of best parameters. We  
426 highlight acceptable sets of parameters in blue while red values correspond to settings  
427 that should not be used. Settings highlighted in green allow more than 90% of the  
428 detected pixels to be corrected. The algorithm performs the best when  $p_{flux} = 50\%$ ,  
429 whatever the value of  $p_{mc}$ . However, for  $p_{flux} \leq 30\%$ , the performances slightly  
430 deteriorate for decreasing  $p_{flux}$ . Although still very acceptable for  $p_{flux} = 30\%$ , the  
431 performances are less good for  $p_{flux} = 10\%$ , especially if  $p_{mc}$  is small. Surprisingly,  
432 for  $p_{flux}$  between 10% and 50%, CorPhU still performs well even without the second  
433 step (see last line of Table 2).

434 For  $p_{flux} \geq 70\%$ , performances degrade with increasing  $p_{flux}$ . In particular, for  
435  $p_{flux} > 1$  (only step 2), the percentage of corrected pixels drops under 35%. When  
436  $p_{flux}$  increases, less corrections are possible with step 1 so CorPhU moves to step 2  
437 to determine the wrong interferogram. The loss of performance suggests that step 2  
438 is less effective than step 1 and that relying only on step 2 degrades the performances  
439 of CorPhU in our case. This suggests that many efficient corrections due to step 1  
440 disappear when  $p_{flux}$  is too high. It should be noted however that the poor performance  
441 of the second step in the Lebanon case may be due to the relatively small number of  
442 triplets as a greater number of triplets should enhance the robustness of the second step.  
443 In general, if  $p_{flux}$  is set between 10% and 50% and  $p_{mc}$  between 30% and 90%, at  
444 least 85% of the pixels are corrected.

445 Nonetheless, analysis of this difference might not be a perfect assessment method  
446 for several reasons. First, some unwrapping errors cannot be detected by triplet misclo-  
447 sure, because the interferogram does not belong to any triplet or because of the masked  
448 areas. Second, errors cannot be detected either when two interferograms of the same  
449 triplet contain on a common region errors that compensate each other in the closure.  
450 This is the case when one acquisition of the triplet contains a sharp atmospheric de-  
451 lay incorrectly unwrapped in two interferograms. Third, the true parameter of interest

452 would be the total number of incorrectly unwrapped pixels on all interferograms. In-  
453 stead,  $W$  counts several times the same error of an interferogram as soon as it belongs  
454 to several triplets. Thus there is no simple relationship between these two variables.  
455 Fourth, if the misclosure of a triplet disappears after the run, it is hopefully due to  
456 a right correction but it also may be due to an incorrect correction. Although such  
457 a wrong correction may then increase the number of pixels with non-zero closure on  
458 other triplets, it is not always the case. Nonetheless,  $W$  seems to vary for a given range  
459 of parameters and tendencies arises, hence it is a proxy of the performance of CorPhU.

460 Even if this parametric analysis is partial, some conclusions can be drawn: the  
461 most determining factor is  $p_{flux}$  which should be set ideally around 50% whereas  $p_{mc}$   
462 should lie above 30%. However, these results are relative to a specific dataset, hence  
463 they should be taken with caution if applied to another dataset. Among others, the  
464 number of interferograms and triplets, the multilooking factors, the shape and size of  
465 decorrelating areas should influence the optimal choice of parameters. A solution to  
466 determine the best set of parameters for a given dataset would be to first run CorPhU  
467 for different sets of parameters in order to make an automatic diagnosis. The algo-  
468 rithm should then be run again with appropriate values of parameters. Another solution  
469 would be to vary the parameters settings during the iterations. The thresholds could be  
470 set to high values during the first iterations to allow only few corrections with a high  
471 confidence level and progressively decrease during the following iterations. The aim  
472 is to avoid any false corrections at the beginning of the process that may later induce  
473 other false corrections.

### 474 **4.3 Effectiveness of the algorithm in correcting unwrapping errors** 475 **in high redundancy datasets**

476 We also assess the effectiveness of the algorithm in correcting unwrapping errors in  
477 large datasets using the proxy  $W$ , corresponding to the total number of pixels on all

478 triplets with non-zero closure (unwrapping errors) automatically computed before and  
479 after two successive runs. We run the algorithm four times, iteratively, on the 686 in-  
480 terferograms of the Turkey dataset. Before performing any corrections, the algorithm  
481 detects around 2 millions of pixels incorrectly unwrapped on the 2880 triplets built  
482 (Figure 8). At the end of the first run, the number of pixels corresponding to unwrap-  
483 ping errors is about 500000, indicating that the algorithm corrects 75% of the initial  
484 pixels in a single iteration. At the end of the second run, the number of pixels de-  
485 creases to 100000, illustrating that the algorithm corrects 95% of the initial incorrectly  
486 unwrapped pixels in only two iterations. Next runs show that the algorithm converge in  
487 two iterations, as the number of pixels incorrectly unwrapped does not decrease any-  
488 more after the second run. This might be due to the size of residual errors, too small to  
489 be corrected considering our threshold, for this particular case, of a minimum 200 pix-  
490 els for a single unwrapping error, or to errors which are not or no longer connected to  
491 references regions (no misclosure), and therefore where the flux method cannot be per-  
492 formed. As a conclusion, the strength of this algorithm is that it automatically corrects  
493 almost all of the unwrapping errors from a large dataset in only two iterations.

#### 494 **4.4 Effectiveness of the algorithm in correcting unwrapping errors** 495 **using a least-square unwrapping method**

496 We test our algorithm not only on interferograms unwrapped using a branch-cut method  
497 but also on those unwrapped using a least-square approach. We unwrap the 686 inter-  
498 ferograms of the Turkey dataset using the Snaphu algorithm and run the algorithm four  
499 times as described above. Before performing any corrections, the algorithm detects  
500 around 20 millions of pixels incorrectly unwrapped on the 2880 triplets built, com-  
501 pared to the 2 millions of pixels for the branch-cut method (Figure 9). At the end of the  
502 first run, the number of pixels corresponding to unwrapping errors does not decrease  
503 significantly, as only 20000 pixels have been corrected during the iteration. Other iter-

504 ations do not lead to perform a high number of corrections.

505       Results suggest that the algorithm is not adapted for interferograms unwrapped using  
506 a least-square approach, such as Snaphu. First, as Snaphu is a global minimization  
507 procedure, resulting triplets phase closure maps are not obvious to interpret, compared  
508 to those computed for interferograms unwrapped using a branch-cut method. Closure  
509 maps are equal to 0 plus or minus a residual that might not necessarily equal a  
510 multiple of  $2\pi$ . Therefore, the algorithm detects, in this case, ten times more pixels  
511 incorrectly unwrapped with Snaphu than with the branch-cut method. Second, global  
512 minimization leads to a less marked spatial signature of unwrapping errors (lower phase  
513 gradients between outer and inner pixels of an unwrapping error). Consequently, the  
514 so-called flux method of our algorithm, designed for the detection of unwrapping errors  
515 using phase gradients, fails most of the time. The mean closure method also fails  
516 most of the time in correcting unwrapping errors because errors are not necessarily a  
517 multiple of  $2\pi$ . Further work is required to adapt our method to global minimization  
518 unwrapping methods.

## 519 **5 Conclusions, limits and future work**

520 We developed an algorithm called CorPhU, using phase closure of triplets of interfero-  
521 grams to correct unwrapping errors left after phase unwrapping. We assess its effi-  
522 ciency on two datasets in Lebanon and Turkey, respectively with Envisat and Sentinel-1  
523 satellites. Our algorithm helps the interpretation of the interferometric phase in low co-  
524 herence regions, polluted by unwrapping errors, without requiring visual interferogram  
525 inspection or manual deletions of unwrapping errors. As the contribution of unwrap-  
526 ping errors to velocity maps may reach up to 1 cm/yr and as they lead to RMS errors  
527 up to 1 cm, it is critical to correct these errors for interseismic strain measurements  
528 in active tectonic environments, where deformation rates are typically on the order of  
529 millimeters per year.

530 As the algorithm is based on triplet information, the more interferograms are con-  
531 structed, the largest the network of triplets is built, hence the higher the probability to  
532 correct recurrent unwrapping errors. The algorithm is particularly powerful for large  
533 datasets such as from Sentinel-1, where the revisit time is 6 days hence allowing to  
534 construct large networks. However, there are some limitations. Processing time is  
535 one of the main constraints and depends on the size of the dataset. For example, the  
536 algorithm takes about six hours to process the Turkey dataset, which corresponds to  
537 2880 triplets, using 24 threads on a classic desktop machine. One way to increase the  
538 speed of processing is to take more benefits from triplets information considering the  
539 first iteration. The goal is to determine which interferograms to correct first so that it  
540 helps for the correction of other interferograms, hence reducing processing time. For  
541 instance, triplets with small-baseline interferograms should be corrected in priority as  
542 they are supposed to be less affected by decorrelation and therefore less affected by un-  
543 wrapping errors. Long-baseline interferograms should be corrected afterwards, using  
544 triplets where small-baseline interferograms have been corrected. Another improve-  
545 ment would be to parallelize some of the steps of the algorithm, for instance to deal  
546 with independent triplets in parallel.

547 Our automatic method, designed for dense networks of interferograms, requires  
548 technical improvements but, in overall, fits well into existing lines of research, where  
549 we increasingly face “big data” related challenges, which must be converted from a  
550 highway to hell to a stairway to heaven.

## 551 **6 Acknowledgments**

552 This project received fundings from the European Research Council (ERC) under the  
553 European Union’s Horizon 2020 research and innovation program (Geo-4D project,  
554 grant agreement 758210). We use the Sentinel-1 and Envisat products, respectively  
555 provided by the Plateforme d’Exploitation des Produits Sentinel (PEPS) for Turkey

556 and ESA through Cat1 proposal and EOLi-SA platform for Lebanon. We process ac-  
557 quisitions using the ISCE system developed at JPL/Caltech (Turkey) and NSBAS chain  
558 based on ROI\_PAC as well (Lebanon). This work was partially supported by The Labo-  
559 ratoire de Recherche Commun Yves Rocard. Data analysis on Lebanon was supported  
560 by CNES through the TOSCA program. The code of our open-source algorithm is  
561 available on Github (<https://github.com/AngeliqueBenoit/CorPhU>).

## 562 **References**

- 563 Agram, P., Jolivet, R., & Simons, M., 2012. Generic InSAR Analysis Toolbox (GIAN-T)  
564 - User Guide, <http://earthdef.caltech.edu>.
- 565 Agram, P. S. & Zebker, H., 2010. Edgelist phase unwrapping algorithm for time series  
566 InSAR analysis, *J. Opt. Soc. Am. A*, **27**(3).
- 567 Cavalié, O., Doin, M.-P., Lasserre, C., & Briole, P., 2007. Ground motion measurement  
568 in the Lake Mead area, Nevada, by differential synthetic aperture radar interferom-  
569 etry time series analysis: Probing the lithosphere rheological structure, *J. Geophys.*  
570 *Res.*, **112**(B3).
- 571 Chen, C. W. & Zebker, H. A., 2001. Two-dimensional phase unwrapping with use of  
572 statistical models for cost functions in nonlinear optimization, *J. Opt. Soc. Am. A*,  
573 **18**(2), 338–351.
- 574 Costantini, M., 1998. A novel phase unwrapping method based on network program-  
575 ming, *IEEE Trans. Geosci. Remote Sens.*, **36**(3), 813–821.
- 576 De Zan, F., Zonno, M., & Lopez-Dekker, P., 2015. Phase Inconsistencies and Multiple  
577 Scattering in SAR Interferometry, *IEEE Trans. Geosci. Remote Sens.*, **53**(12), 6608–  
578 6616.
- 579 Doin, M.-P., Lasserre, C., Peltzer, G., Cavalié, O., & Doubre, C., 2009. Corrections of  
580 stratified tropospheric delays in SAR interferometry: Validation with global atmo-  
581 spheric models, *J. Appl. Geophys.*, **69**(1), 35–50.
- 582 Doin, M.-P., Lodge, F., Guillaso, S., Jolivet, R., Lasserre, C., Ducret, G., Grandin, R.,  
583 Pathier, E., & Pinel, V., 2011. Presentation of the small baseline NSBAS processing  
584 chain on a case example: the Etna deformation monitoring from 2003 to 2010 using  
585 Envisat data, *Proc. ESA 'Fringe 2011 Work. Frascati, Italy, (19-23 Sept. 2011)*, pp.  
586 19–23.
- 587 Ducret, G., Doin, M.-P., Grandin, R., Lasserre, C., & Guillaso, S., 2014. DEM Cor-  
588 rections Before Unwrapping in a Small Baseline Strategy for InSAR Time Series  
589 Analysis, *IEEE Geosci. Remote Sens. Lett.*, **11**(3), 696–700.



- 590 Elias, A., Tapponnier, P., Singh, S. C., King, G. C., Briais, A., Daëron, M., Carton, H.,  
591 Sursock, A., Jacques, E., Jomaa, R., & Klinger, Y., 2007. Active thrusting offshore  
592 Mount Lebanon: Source of the tsunamigenic A.D. 551 Beirut-Tripoli earthquake,  
593 *Geology*, **35**(8).
- 594 Elliott, J., Walters, R., & Wright, T., 2016. The role of space-based observation in  
595 understanding and responding to active tectonics and earthquakes, *Nat. Commun.*,  
596 **7**(1).
- 597 Farr, T. G., Rosen, P. A., Caro, E., Crippen, R., Duren, R., Hensley, S., Kobrick, M.,  
598 Paller, M., Rodriguez, E., Roth, L., Seal, D., Shaffer, S., Shimada, J., Umland, J.,  
599 Werner, M., Oskin, M., Burbank, D., & Alsdorf, D., 2007. The Shuttle Radar To-  
600 pography Mission, *Rev. Geophys.*, **45**(2).
- 601 Fattahi, H., Agram, P., & Simons, M., 2017. A Network-Based Enhanced Spectral  
602 Diversity Approach for TOPS Time-Series Analysis, *IEEE Trans. Geosci. Remote*  
603 *Sens.*, **55**(2), 777–786.
- 604 Flynn, T. J., 1997. Two-dimensional phase unwrapping with minimum weighted dis-  
605 continuity, *J. Opt. Soc. Am. A*, **14**(10).
- 606 Ghiglia, D. C. & Romero, L. A., 1994. Robust two-dimensional weighted and un-  
607 weighted phase unwrapping that uses fast transforms and iterative methods, *J. Opt.*  
608 *Soc. Am. A*, **11**(1).
- 609 Goldstein, R. M. & Werner, C. L., 1998. Radar interferogram filtering for geophysical  
610 applications, *Geophys. Res. Lett.*, **25**(21), 4035–4038.
- 611 Goldstein, R. M., Zebker, H. A., & Werner, C. L., 1988. Satellite radar interferometry:  
612 Two-dimensional phase unwrapping, *Radio Sci.*, **23**(4), 713–720.
- 613 Goldstein, R. M., Engelhardt, H., Kamb, B., & Frolich, R. M., 1993. Satellite Radar  
614 Interferometry for Monitoring Ice Sheet Motion: Application to an Antarctic Ice  
615 Stream, *Science (80-. )*, **262**(5139), 1525–1530.
- 616 Graham, L., 1974. Synthetic interferometer radar for topographic mapping, *Proc.*  
617 *IEEE*, **62**(6), 763–768.
- 618 Guillaso, S., Lasserre, C., Doin, M.-P., Cavalie, O., Sun, J., & Pelzer, G., 2008. InSAR  
619 measurement of interseismic strain in areas of low coherence: example across the  
620 Haiyuan fault (Gansu, China) using a local InSAR adaptive range filter, *EGU*, **10**.
- 621 Gurrola, E., Rosen, P. A., Sacco, G. F., Seliga, W., Zebker, H., Simons, M., & Sandwell,  
622 D., 2010. InSAR Scientific Computing Environment, *2010 Am. Geophys. Union*  
623 *Meet.*.
- 624 Hersbach, H. & Dee, D., 2016. ERA5 reanalysis is in production, *ECMWF Newsl.*,  
625 **147**.
- 626 Herzterg, I., Poggi, M., & Vidal, T., 2018. 2D-Phase Unwrapping via Balanced Span-  
627 ning Forests, (1995).

- 628 Hooper, A. & Zebker, H. A., 2007. Phase unwrapping in three dimensions with appli-  
629 cation to InSAR time series, *J. Opt. Soc. Am. A*, **24**(9).
- 630 Hussain, E., Hooper, A., Wright, T. J., Walters, R. J., & Bekaert, D. P. S., 2016. In-  
631 terseismic strain accumulation across the central North Anatolian Fault from iter-  
632 atively unwrapped InSAR measurements, *J. Geophys. Res. Solid Earth*, **121**(12),  
633 9000–9019.
- 634 Jennison, R. C., 1958. A Phase Sensitive Interferometer Technique for the Measure-  
635 ment of the Fourier Transforms of Spatial Brightness Distributions of Small Angular  
636 Extent, *Mon. Not. R. Astron. Soc.*, **118**(3), 276–284.
- 637 Jolivet, R., Grandin, R., Lasserre, C., Doin, M.-P., & Peltzer, G., 2011. Systematic  
638 InSAR tropospheric phase delay corrections from global meteorological reanalysis  
639 data, *Geophys. Res. Lett.*, **38**(17).
- 640 Jolivet, R., Lasserre, C., Doin, M.-P., Guillaso, S., Peltzer, G., Dailu, R., Sun, J., Shen,  
641 Z.-K., & Xu, X., 2012. Shallow creep on the Haiyuan Fault (Gansu, China) revealed  
642 by SAR Interferometry, *J. Geophys. Res. Solid Earth*, **117**(B6).
- 643 Lee, J., Hoppel, K., Mango, S., & Miller, A., 1994. Intensity and phase statistics  
644 of multilook polarimetric and interferometric SAR imagery, *IEEE Trans. Geosci.*  
645 *Remote Sens.*, **32**(4), 1017–1028.
- 646 Lin, Q., Vesecky, J. F., & Zebker, H. A., 1994. Phase unwrapping through fringe-line  
647 detection in synthetic aperture radar interferometry, *Appl. Opt.*, **33**(2).
- 648 Lin, Y.-n. N., Simons, M., Hetland, E. A., Muse, P., & DiCaprio, C., 2010. A multi-  
649 scale approach to estimating topographically correlated propagation delays in radar  
650 interferograms, *Geochem., Geophys. Geosys.*, **11**(9).
- 651 López-Quiroz, P., Doin, M.-p., Tupin, F., Briole, P., & Nicolas, J.-m., 2009. Time  
652 series analysis of Mexico City subsidence constrained by radar interferometry, *J.*  
653 *Appl. Geophys.*, **69**(1), 1–15.
- 654 Margot, J.-L., Campbell, D., Jurgens, R., & Slade, M., 2000. Digital elevation models  
655 of the Moon from Earth-based radar interferometry, *IEEE Trans. Geosci. Remote*  
656 *Sens.*, **38**(2), 1122–1133.
- 657 Massonnet, D., Rossi, M., Carmona, C., Adragna, F., Peltzer, G., Feigl, K., & Rabaute,  
658 T., 1993. The displacement field of the Landers earthquake mapped by radar inter-  
659 ferometry, *Nature*, **364**(6433), 138–142.
- 660 Massonnet, D., Briole, P., & Arnaud, A., 1995. Deflation of Mount Etna monitored by  
661 spaceborne radar interferometry, *Nature*, **375**(6532), 567–570.
- 662 Matheron, G., 1967. *Elements pour une theorie des milieux poreux*, Paris, masson edn.
- 663 Pepe, A. & Lanari, R., 2006. On the Extension of the Minimum Cost Flow Algorithm  
664 for Phase Unwrapping of Multitemporal Differential SAR Interferograms, *IEEE*  
665 *Trans. Geosci. Remote Sens.*, **44**(9), 2374–2383.

- 666 Pinel-Puysségur, B., Michel, R., & Avouac, J.-P., 2012. Multi-Link InSAR Time Series: Enhancement of a Wrapped Interferometric Database, *IEEE J. Sel. Top. Appl. Earth Obs. Remote Sens.*, **5**(3), 784–794.
- 669 Pinel-Puysségur, B., Lasserre, C., Benoit, A., Jolivet, R., Doin, M.-p., & Champenois, J., 2018. A Simple Phase Unwrapping Errors Correction Algorithm Based on Phase Closure Analysis, in *IGARSS 2018 - 2018 IEEE Int. Geosci. Remote Sens. Symp.*, vol. 1, pp. 2212–2215, IEEE.
- 673 Prati, C., Giani, M., & Leuratti, N., 1990. SAR Interferometry: A 2-D Phase Unwrapping Technique Based On Phase And Absolute Values Informations, in *10th Annu. Int. Symp. Geosci. Remote Sens.*, pp. 2043–2046, IEEE.
- 676 Reilinger, R. E., Ergintav, S., Bürgmann, R., McClusky, S., Lenk, O., Barka, A., Gurkan, O., Hearn, L., Feigl, K. L., Cakmak, R., Aktug, B., Ozener, H., & Töksoz, M. N., 2000. Coseismic and Postseismic Fault Slip for the 17 August 1999, M = 7.5, Izmit, Turkey Earthquake, *Science (80-. )*, **289**(5484), 1519–1524.
- 680 Rogers, A. E. E. & Ingalls, R. P., 1970. Radar Mapping of Venus With Interferometric Resolution of the Range-Doppler Ambiguity, *Radio Sci.*, **5**(2), 425–433.
- 682 Rosen, P. A., Hensley, S., Zebker, H. A., Webb, F. H., & Fielding, E. J., 1996. Surface deformation and coherence measurements of Kilauea Volcano, Hawaii, from SIR-C radar interferometry, *J. Geophys. Res.*, **101**(E10).
- 685 Rosen, P. A., Hensley, S., Peltzer, G., & Simons, M., 2004. Updated repeat orbit interferometry package released, *Eos, Trans. Am. Geophys. Union*, **85**(5).
- 687 Simons, M. & Rosen, P., 2015. Interferometric Synthetic Aperture Radar Geodesy, in *Treatise Geophys.*, vol. 3, pp. 339–385, Elsevier.
- 689 Simons, M., Fialko, Y., & Riviera, L., 2002. Coseismic Deformation from the 1999 Mw 7.1 Hector Mine, California, Earthquake as Inferred from InSAR and GPS Observations, *Bull. Seismol. Soc. Am.*, **92**(4), 1390–1402.
- 692 Stein, R. S., Barka, A. A., & Dieterich, J. H., 1997. Progressive failure on the North Anatolian fault since 1939 by earthquake stress triggering, *Geophys. J. Int.*, **128**(3), 594–604.
- 695 Verveer, P., 2003. GitHub repository, SciPy library.
- 696 Zebker, H., Shankar, P., & Hooper, A., 2007. InSAR Remote Sensing Over Decorrelating Terrains: Persistent Scattering Methods, in *2007 IEEE Radar Conf.*, pp. 717–722, IEEE.
- 699 Zebker, H. A. & Goldstein, R. M., 1986. Topographic mapping from interferometric synthetic aperture radar observations, *J. Geophys. Res.*, **91**(B5), 4993–4999.
- 701 Zebker, H. A., Rosen, P. A., Goldstein, R. M., Gabriel, A., & Werner, C. L., 1994. On the derivation of coseismic displacement fields using differential radar interferometry: The Landers earthquake, *J. Geophys. Res. Solid Earth*, **99**(B10).

- 704 Zisk, S. H., 1972a. Lunar Topography: First Radar-Interferometer Measurements of  
705 the Alphonsus-Ptolemaeus-Arzachel Region, *Science* (80-. ), **178**(4064), 977–980.
- 706 Zisk, S. H., 1972b. A new, earth-based radar technique for the measurement of lunar  
707 topography, *Moon*, **4**(3-4), 296–306.

Table 1: Default values for the algorithm thresholds.

Name	Value (default)
$minSize$	200
$pflux$	30%
$p_{mc}$	50%
$r_{mc}$	2

Table 2: Percentage of corrected pixels for the 35 parametric tests performed on the Lebanon dataset. Column  $p_{flux} > 100\%$  (respectively  $p_{mc} > 100\%$ ) corresponds to step 2 (resp. step 1) only. NA: not applicable.

$p_{mc} \backslash p_{flux}$	10%	30%	50%	70%	90%	>100%
10%	51.24	87.57	91.88	83.30	70.52	34.28
30%	87.83	87.49	90.83	83.16	40.22	7.89
50%	87.72	87.27	90.66	83.12	39.76	8.07
70%	87.36	86.99	90.52	83.29	45.66	13.30
90%	87.25	86.71	90.30	82.90	44.20	11.97
>100%	91.25	90.49	81.92	44.45	8.85	NA

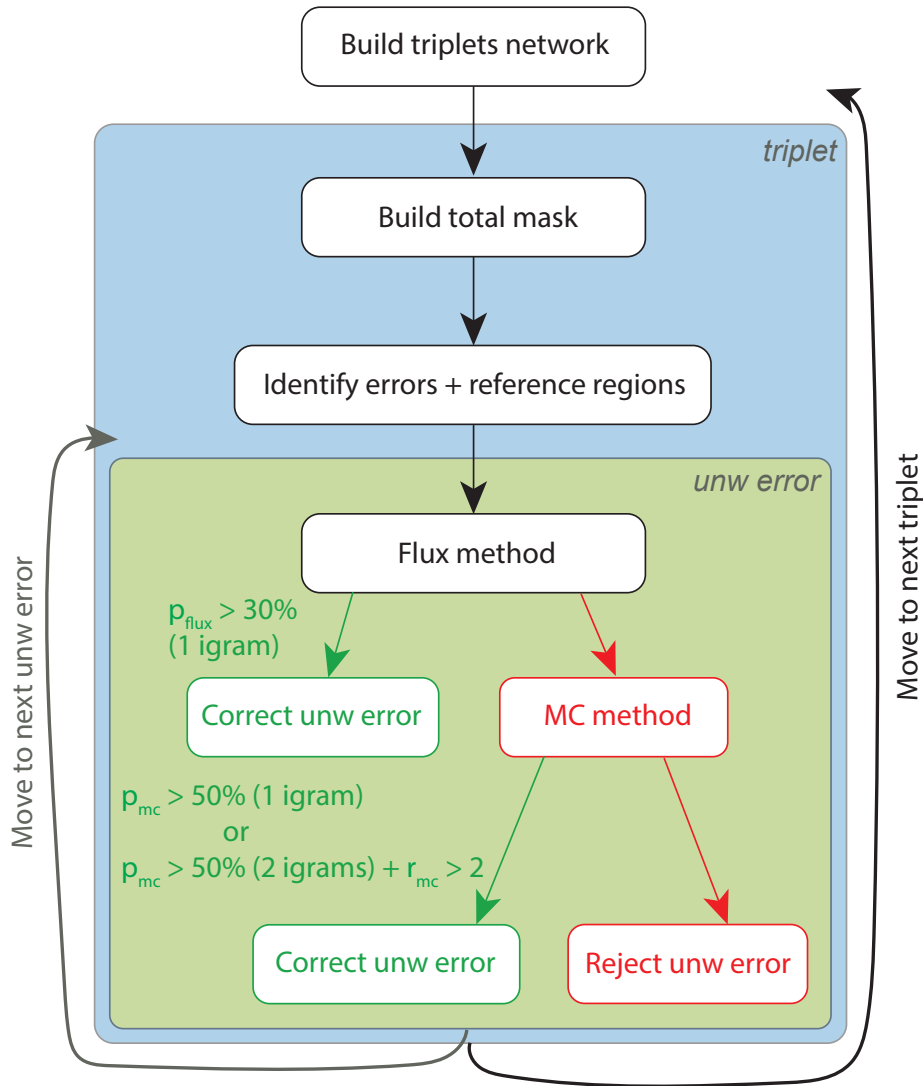


Figure 1: Algorithm implementation. First, we build the network of triplets. We process then each triplet. We identify unwrapping errors and reference regions using triplet phase closure. We correct each unwrapping error using a two-steps detection, with the flux method or with the mean closure method, in case the flux method cannot determine which interferogram to correct.

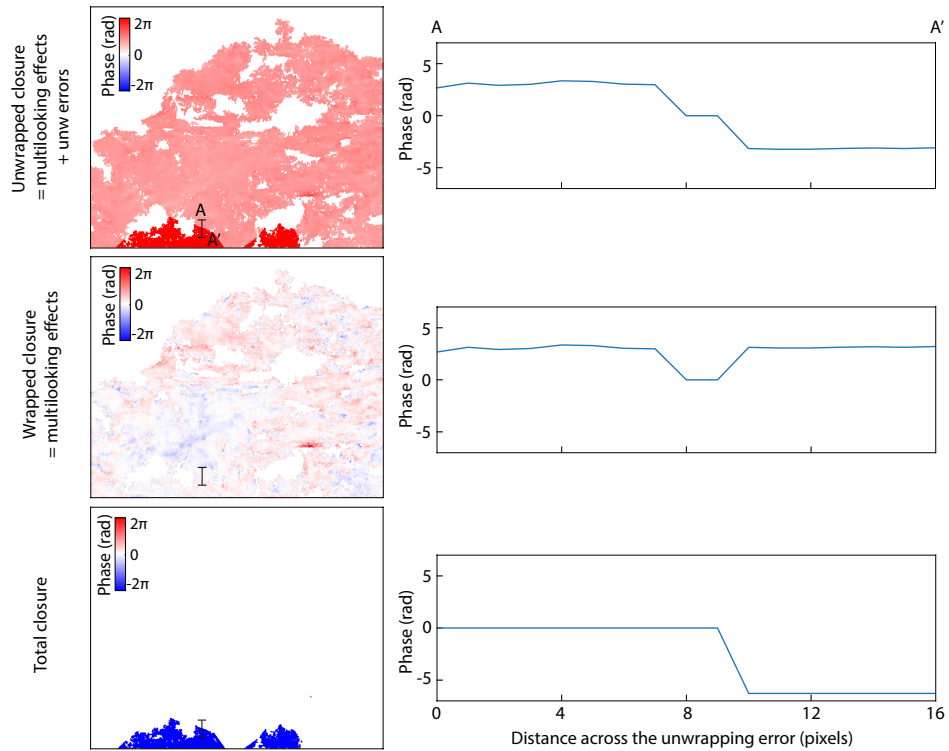


Figure 2: Closure maps (left) and profiles across an unwrapping error (right). Top) Closure from unwrapped interferograms. Center) Closure from wrapped interferograms. Non zero closure is due to multilooking. Bottom) Total closure computed by removing misclosures due to multilooking effects.

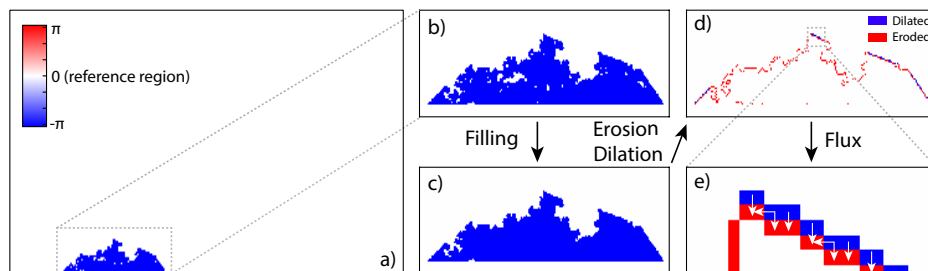


Figure 3: Steps to identify and correct an unwrapping error by the so-called flux method. a) Total phase closure of the triplet. b-c) Masked pixels within the unwrapping error zone are filled by erosion and dilation tool. d) Erosion and dilation of the unwrapping error zone to identify inner (red) and outer (blue) border. e) Computation of flux vectors between outer and inner pixels of the unwrapping error.

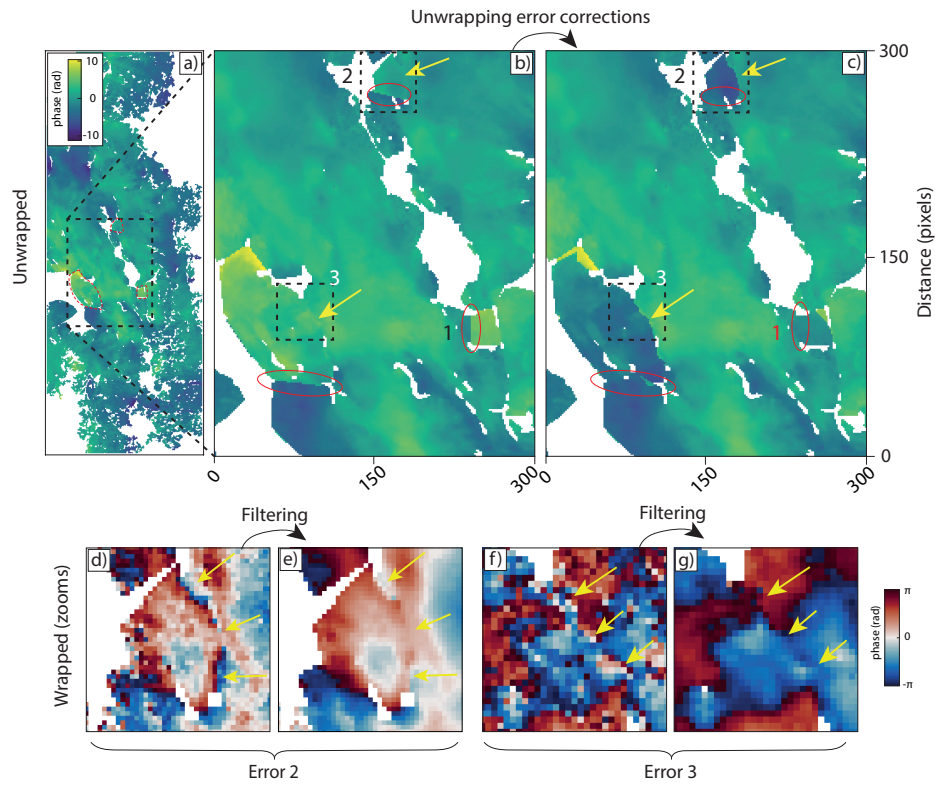


Figure 4: Results for Envisat dataset in Lebanon. a) Example of an interferogram spanning 2004/08/01 - 2008/07/06 which contains unwrapping errors (red circles). b) and c) Zooms of not corrected and corrected unwrapped interferograms. Error 1 is well corrected by the algorithm. Errors 2 and 3 are challenging areas, where the high fringe gradient, visible on wrapped interferograms, disappears by filtering before unwrapping (arrows in b). The algorithm restores the correct positions of offsets (arrows in c). d), e), f) and g) Zooms of unwrapping errors 2 and 3 on wrapped interferograms, before and after filtering. Filtering erases fringes in high fringe rate regions (arrows).



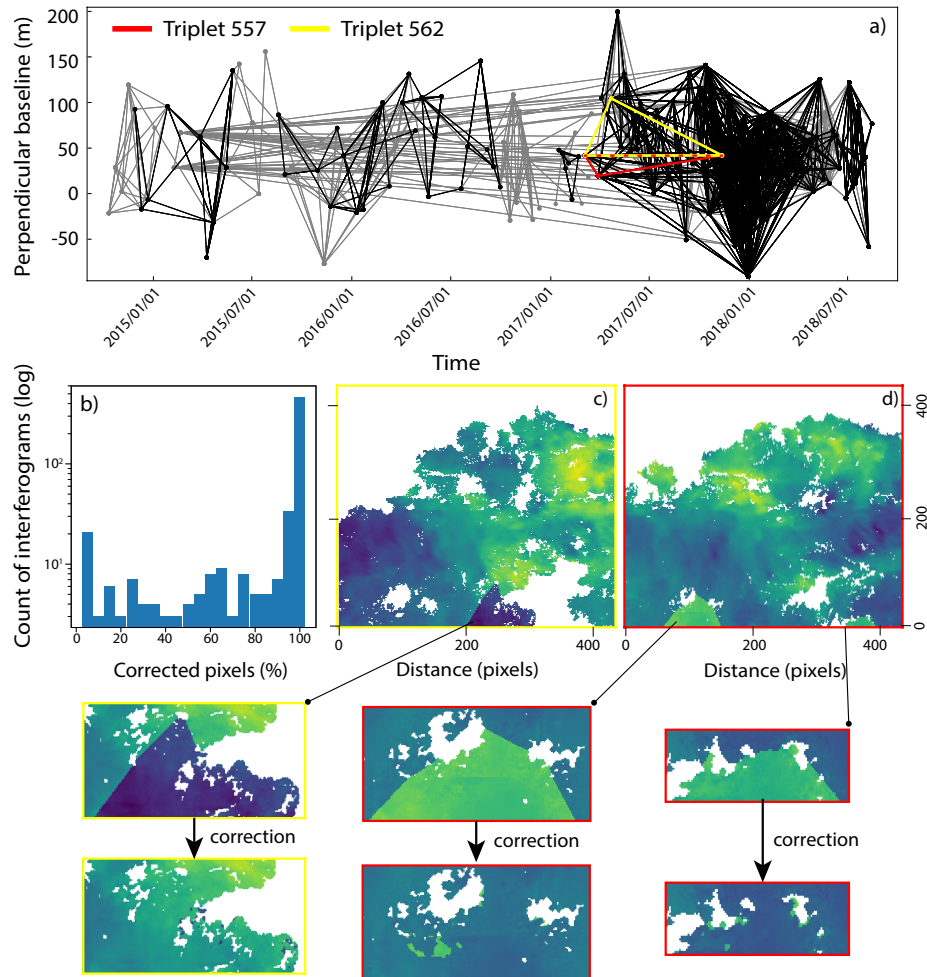


Figure 5: Results for Sentinel-1 dataset in Turkey. a) Perpendicular baseline plot with corrected triplets in black. Dots are SAR acquisitions and lines are interferograms. b) Histogram of the number of interferograms corrected as a function of percentage of corrected pixels. c) and d) Examples of corrections spanning 2017/04/22 - 2017/11/12 and 2017/03/05 - 2017/11/12, respectively.

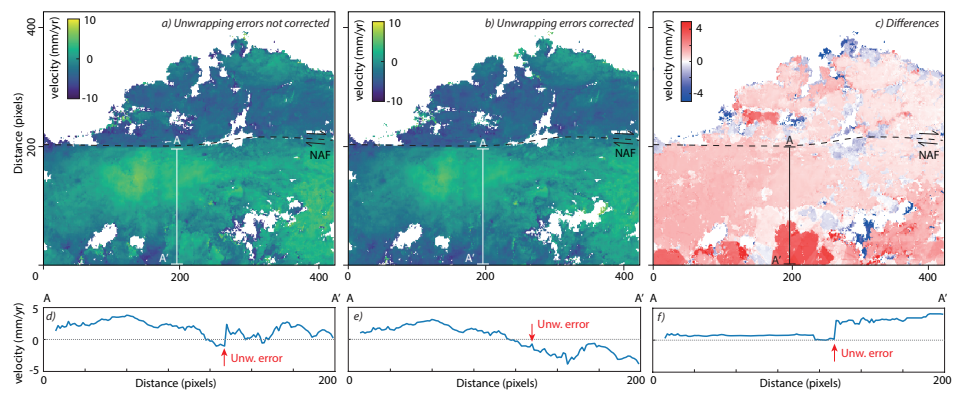


Figure 6: Influence of unwrapping error corrections on time series analysis. a) Velocity map calculated from a stack of interferograms not corrected from unwrapping errors and b) from a stack of interferograms corrected from unwrapping errors. c) Differences between a and b. d) e) and f) Profiles across a, b and c, respectively.

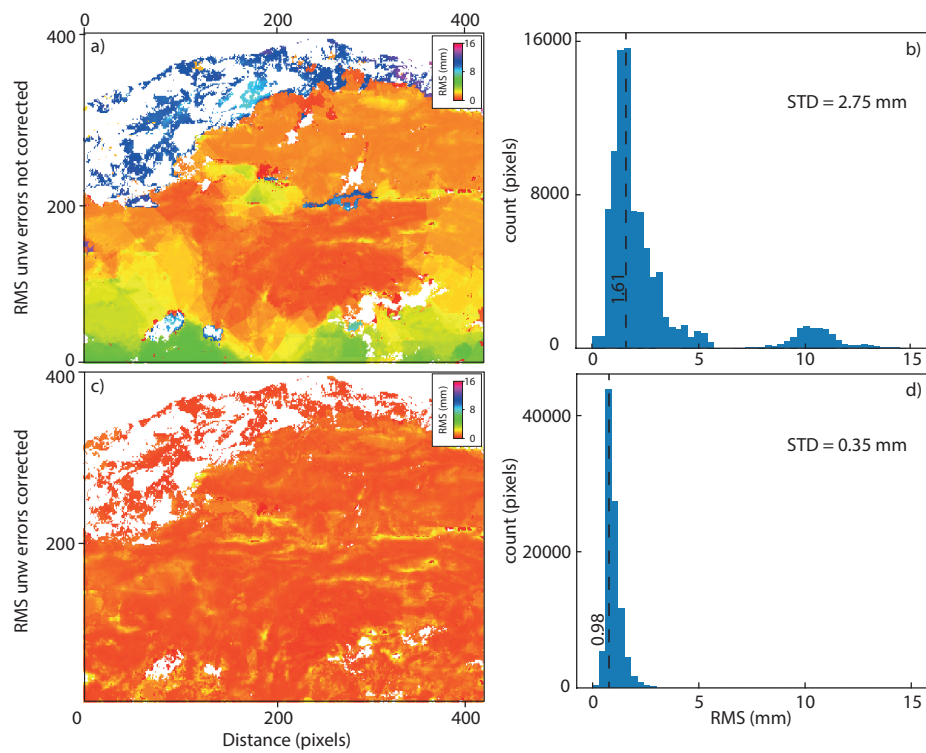


Figure 7: Influence of unwrapping errors on root mean square (RMS) maps. a) and c) RMS maps where unwrapping errors are not corrected and corrected, respectively. Unwrapping errors have a large contribution on the estimation of RMS. b) and d) Histograms of RMS maps a and c, respectively.

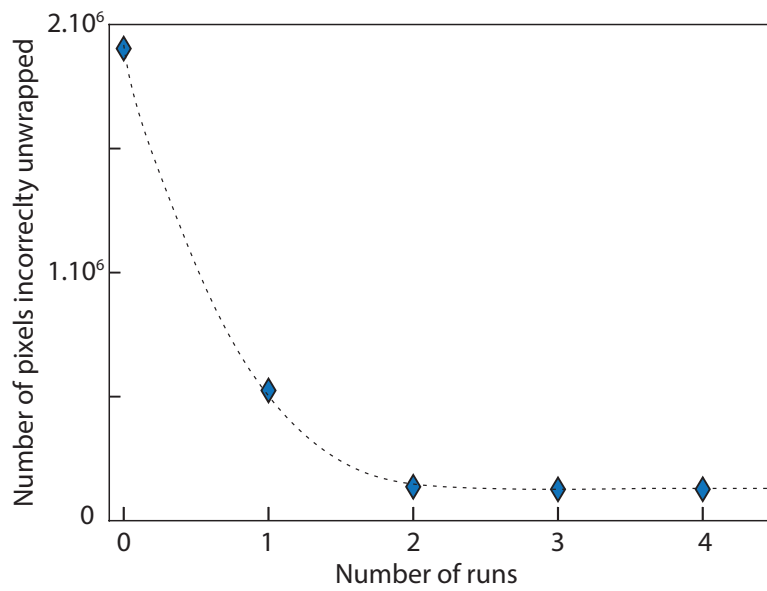


Figure 8: Number of pixels incorrectly unwrapped by a branch-cut method (unwrapping errors) detected by the algorithm during 4 successive runs. The algorithm converge in two iterations, leading to correct 95% of the 2 millions pixels incorrectly unwrapped at the beginning.

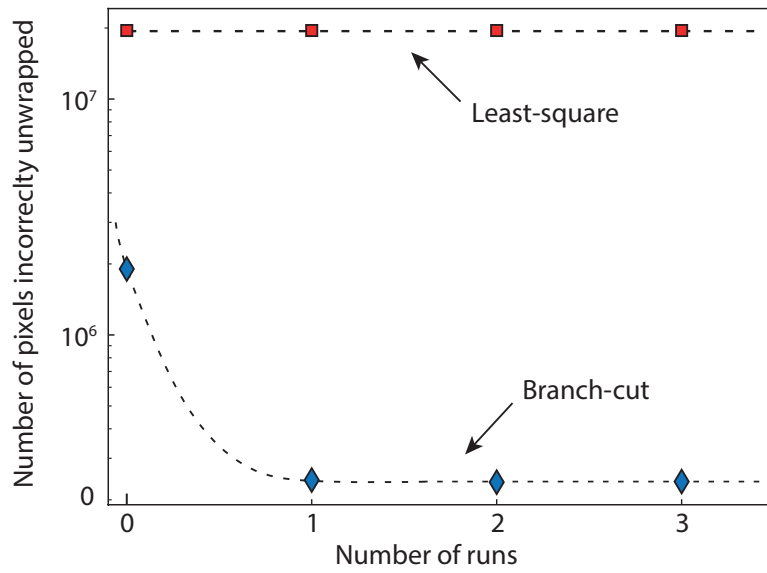


Figure 9: Comparison of the number of pixels incorrectly unwrapped by a branch-cut (blue diamonds) and a least-square (red squares) approach detected by the algorithm during 3 successive runs.